Electronic Supplementary Material (ESI) for Journal of Materials Chemistry C.

Supplementary Information for "Towards high-throughput exciton diffusion rate prediction in molecular organic semiconductors"

Geoffrey R. Weal,[†,‡,¶,§] Joshua J. Sutton,[†,§] Chayanit Wechwithayakhlung,[†,‡,¶] Daniel M. Packwood,[†,‡,¶] Justin M. Hodgkiss,[*,†,¶,§] and Paul A. Hume[*,†,¶,§]

†*School of Chemical and Physical Sciences, Victoria University of Wellington, Wellington, 6010, New Zealand.*

‡*Institute for Integrated Cell-Material Sciences (iCeMS), Kyoto University, Kyoto, Japan.*

¶*Center for Integrated Data-Material Sciences (iDM), MacDiarmid Institute for Advanced Materials and Nanotechnology, Wellington, New Zealand.*

§*MacDiarmid Institute for Advanced Materials and Nanotechnology, Wellington, 6010, New Zealand.*

E-mail: justin.hodgkiss@vuw.ac.nz; paul.hume@vuw.ac.nz

S1 Crystal structure details

Table S1 provides details of the 24 crystal structures for the six fused-ring electron acceptor (FREA) molecules studied in this paper.

Molecule Name	CCDC ID	Space group	Unit Cell a (Å)	b (Å)	c (Å)	α (°)	β (°)	γ (°)	Z	Z'	Reference (DOI)
EH-IDTBR	FOSPUB	$P\bar{1}$	10.0709	12.3721	16.3680	78.476	73.057	66.120	1	0.5	Ref. 1: 10.1002/aelm.201900344
	FOSPOV	$P2_1/c$	13.7663	15.81032	32.7146	90	96.2928	90	4	1	Ref. 1: 10.1002/aelm.201900344
	FOSPOV01	$P2_1/c$	13.7638	15.8480	32.7182	90	96.853	90	4	1	Ref. 2: 10.1021/acs.joc.9b01654
	FOSPOV03	$P2_1/c$	13.730	15.680	32.720	90.00	95.90	90.00	4	1	Ref. 3: 10.1021/acs.chemmater.0c04111
	PUGSIW	$C2/c$	23.1692	31.0397	13.9273	90	105.640	90	4	0.5	Ref. 2: 10.1021/acs.joc.9b01654
IDIC	JOGYUC	$P\bar{1}$	11.7944	17.3479	25.4626	107.7160	94.0560	107.8200	3	1.5	Ref. 4: 10.1021/jacs.8b12982
	VUBKAH	$P\bar{1}$	8.6679	12.5073	13.5784	72.096	75.545	88.839	1	0.5	Ref. 5: 10.1039/C9MH01439J
	VUBKAH01	$P\bar{1}$	8.6238	12.6353	13.9076	70.658	75.065	88.166	1	0.5	Ref. 6: 10.1021/acs.jpclett.0c03260
	VUBKAH02	$P\bar{1}$	14.0557	14.1621	15.9729	99.670	94.2978	100.596	2	1	Ref. 6: 10.1021/acs.jpclett.0c03260
ITIC	HEHQUJ	$P\bar{1}$	14.880	15.470	18.080	99.27	101.50	108.37	2	1	Ref. 7: 10.1039/C7TC01310H
	HEHQUJ01	$P\bar{1}$	14.9009	15.5043	18.1199	99.309	101.541	108.366	2	1	Ref. 5: 10.1039/C9MH01439J
	IVEQAE	$P\bar{1}$	15.7472	16.9033	18.0345	64.976	73.853	84.654	2	1	Ref. 8: 10.1021/acs.jpclett.0c02569
	KIZSUK*	$P\bar{1}$	8.420	23.019	23.126	101.780	95.319	91.105	2	1	Ref. 9: 10.1021/jacs.8b13653
	NULYEB*	$P\bar{1}$	8.7888	18.7534	25.5301	88.9873	88.2993	81.2251	2	1	Ref. 10: 10.1002/cphc.201900793
	VABGIS*	$C2/c$	26.935	27.597	15.723	90	121.893	90	4	0.5	Ref. 11: 10.1021/jacs.0c07083
	VUBJOU*	$P\bar{1}$	8.7454	18.872	25.2647	87.770	88.724	78.001	2	1	Ref. 5: 10.1039/C9MH01439J
ITIC-2Cl (δ)	HOVDEE	$P\bar{1}$	8.4146	19.3808	26.3736	98.102	93.830	102.069	2	1	Ref. 12: 10.1016/j.isci.2019.06.033
ITIC-2Cl (γ)	HOVDAA	$P\bar{1}$	11.0040	27.3249	27.3630	98.245	96.231	98.997	3	1.5	Ref. 12: 10.1016/j.isci.2019.06.033
ITIC-4F	KIZTAR	$P\bar{1}$	15.4222	17.6025	21.1852	73.995	68.809	81.206	2	1	Ref. 9: 10.1021/jacs.8b13653
	KIZTAR01	$P\bar{1}$	15.533	17.735	21.067	100.436	111.562	99.507	2	1	Ref. 11: 10.1021/jacs.0c07083
Y6	MUPMOC	$P\bar{1}$	13.7272	19.6561	29.7056	102.450	92.677	96.570	4	2	Ref. 13: 10.1038/s41467-020-17867-1
	MUVVEH	$P2_1/c$	15.1117	57.812	20.0760	90	95.923	90	8	2	Ref. 14: 10.1021/jacs.0c05560
	MUVVEH01	$P\bar{1}$	14.5264	19.8017	28.5349	95.143	101.463	107.364	4	2	Ref. 15: 10.1002/anie.202105156
	OHEPID	$C2/c$	23.7019	57.450	14.3969	90	118.541	90	8	1	Ref. 11: 10.1021/jacs.0c07083

Table S1: Crystallographic information for the six FREA molecules studied in this paper. * Solvent was include in the crystal structure.

S2 KMC simulations using PCM and range-tuning

To account for potential intramolecular CT character, we also performed a series of calculations employing a range-tuned exchange–correlation functional (according to the non-empirical procedure[16]), as well as using a polarisable continuum model (PCM) as a crude approximation of dielectric effects on the excitonic couplings V_{ij} and reorganisation energy λ. The diffusion coefficients obtained from kinetic Monte-Carlo (kMC) simulations using range-tuning and PCM models are shown:

1. Figure S1: No PCM or range-tuning (equivalent to Figure 4 in the main text, however Figure S1 only includes the diffusion coefficient for one crystal structure for each FREA, rather than all crystal structures).
2. Figure S2: PCM, no range-tuning.
3. Figure S3: Range-tuning, no PCM.
4. Figure S4: PCM and range-tuning.

The crystal structures included in Figures S1 to S4 were FOSPUB (EH-IDTBR),[1] JOGYUC (IDIC),[4] HEHQUJ (ITIC),[7] HOVDEE (ITIC-2Cl (δ)),[12] HOVDAA (ITIC-2Cl (γ)),[12] KIZTAR (ITIC-4F),[9] and MUPMOC (Y6).[13] Experimental diffusion coefficients were obtained using intensity-dependent transient absorption (TA) spectroscopy and thickness-dependent external quantum efficiency measurements in the presence of a quenching layer.[4,17,18] The diffusion coefficient for EH-IDTBR was calculated using the experimentally-reported diffusion length[17] and excited state lifetime measured using time-revolved photoluminescence (TRPL) spectroscopy.[18]

The effect of range-tuning was negligible, while the use of PCM solvation lowered the correlation of our predictions with the experimental values (including when combined with range-tuning).

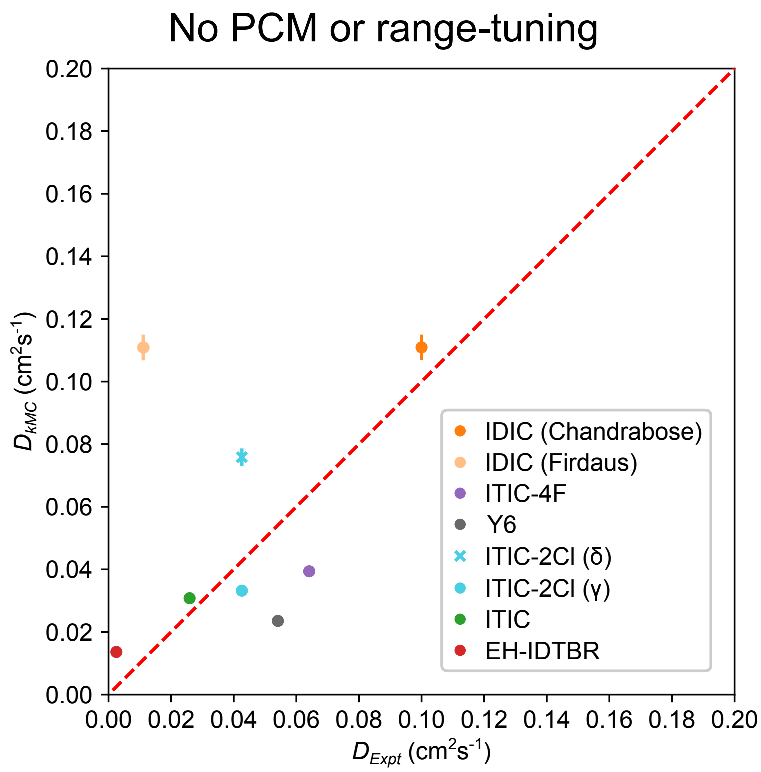

Figure S1: Kinetic Monte-Carlo (kMC) vs. experimental diffusion coefficients (D_{kMC} vs. D_{Expt}) for a series of FREAs. **No PCM or range-tuning was applied in these results**. Points closer to the dashed red line indicate better agreement between the predicted and experimental diffusion rates. Error bars indicate 3× the standard deviation (representing 99.7 % of diffusion coefficients obtained). This figure is equivalent to Figure 4 in the main text, however this figure only includes the diffusion coefficient for one crystal structure of each FREA sampled rather than all crystal structures.

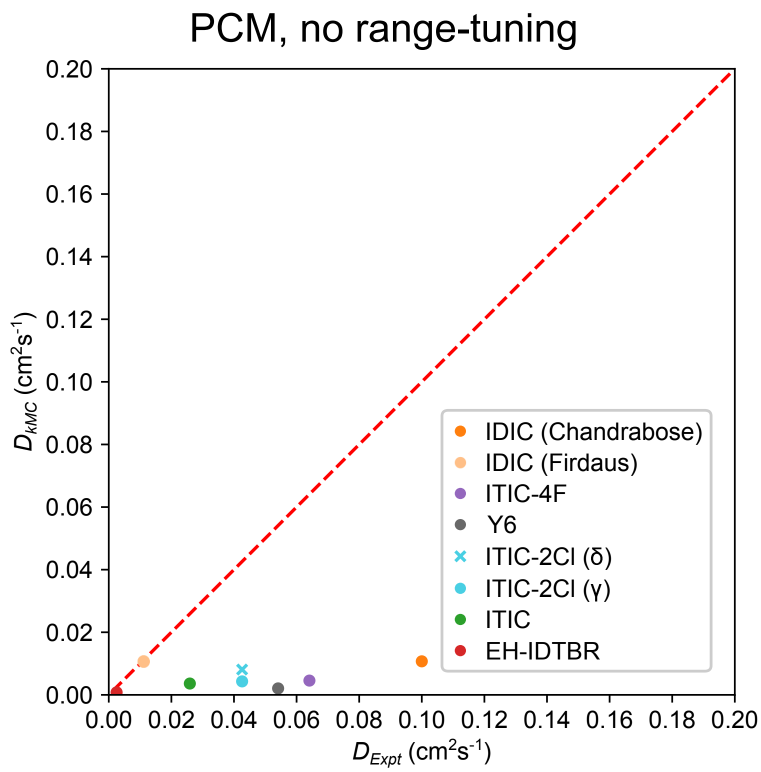

Figure S2: Kinetic Monte-Carlo (kMC) vs. experimental diffusion coefficients (D_{kMC} vs. D_{Expt}) for a series of FREAs. **Only the PCM method was applied in these results**. Points closer to the dashed red line indicate better agreement between the predicted and experimental diffusion rates. Error bars indicate 3× the standard deviation (representing 99.7 % of diffusion coefficients obtained).

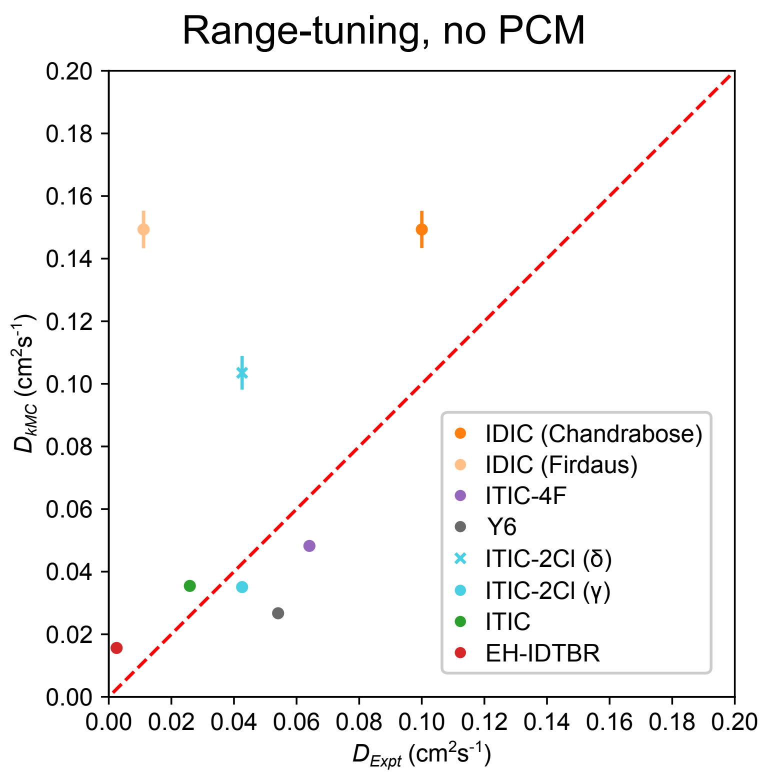

Figure S3: Kinetic Monte-Carlo (kMC) vs. experimental diffusion coefficients (D_{kMC} vs. D_{Expt}) for a series of FREAs. **Only the range-tuning method was applied in these results**. Points closer to the dashed red line indicate better agreement between the predicted and experimental diffusion rates. Error bars indicate $3\times$ the standard deviation (representing 99.7 % of diffusion coefficients obtained).

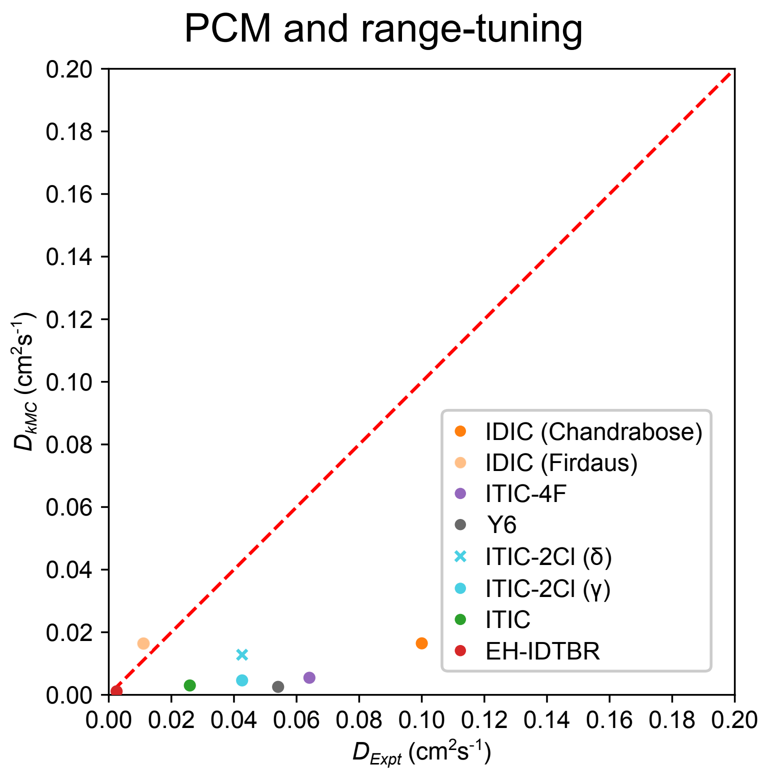

Figure S4: Kinetic Monte-Carlo (kMC) vs. experimental diffusion coefficients (D_{kMC} vs. D_{Expt}) for a series of FREAs. **Both the PCM and range-tuning methods were applied in these results**. Points closer to the dashed red line indicate better agreement between the predicted and experimental diffusion rates. Error bars indicate 3× the standard deviation (representing 99.7 % of diffusion coefficients obtained).

S3 Comparisons of excitonic coupling strength with reorganisation energy

To assess the validity of the incoherent diffusion model used in this work, excitonic coupling values obtained using the EET and ATC methods were compared to the reorganisation energy (λ). For incoherent models to be valid, couplings should be less than $\lambda/4$. Figures S5 and S6 show the EET and ATC coupling values from the OPV materials, respectively. The incoherent limit ($\lambda/4$) is given by the dashed lines in Figures S5 and S6. The data for these figures was obtained from the coupling values given in Figure 7 of the main text, while the reorganisation energies are given in Table 1 of the main text.

All the coupling values are lower or equal to the incoherent limit for all OPV molecules, except for Y6 where two dimers have EET coupling values greater than $\lambda/4$ (Figure S5). These two Y6 dimers can be seen in Figures S7 and S8. OHEPID - dimer 13 in particular has a significant overlap contribution to the EET value (Table S2). As previously noted,[19] the couplings in FREA materials approach the limit of incoherent energy transfer rates. However, as noted in the main text, given our focus on high-throughput screening, we are willing to use an incoherent rate equation as long as reasonably accurate predictions of exciton diffusion rates can still be achieved.

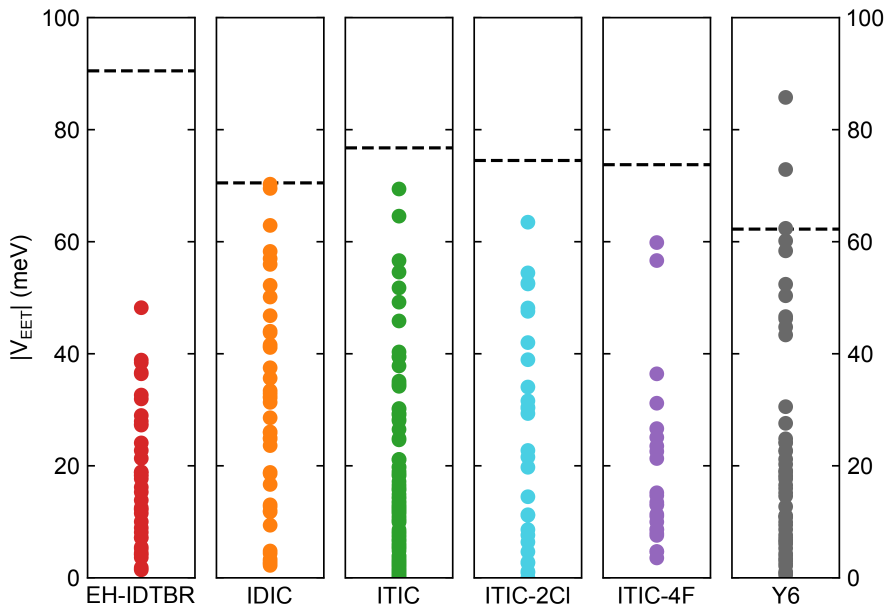

Figure S5: The EET coupling values for all OPV crystal structures examined in this article. The incoherent limit ($\lambda/4$) is given by a dashed line for each OPV material.

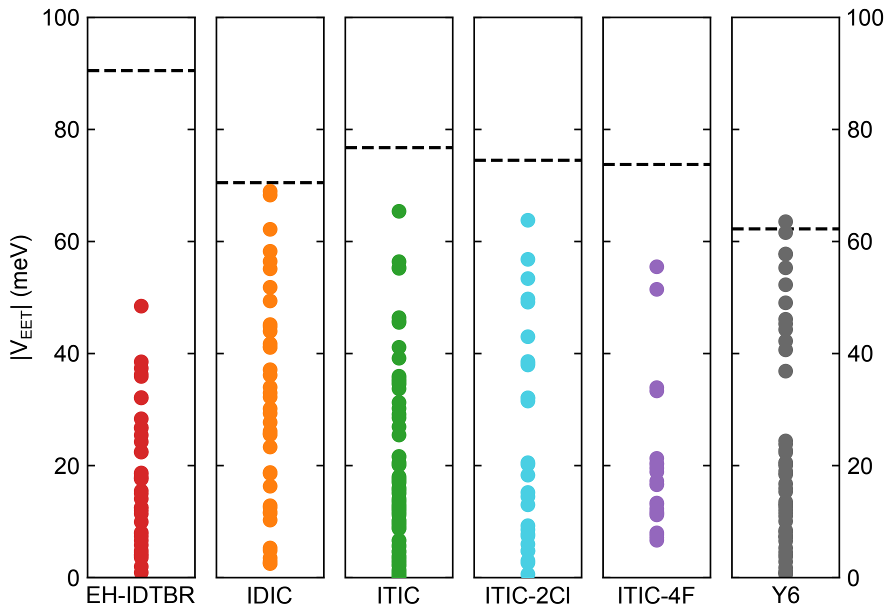

Figure S6: The ATC coupling values for all OPV crystal structures examined in this article. The incoherent limit ($\lambda/4$) is given by a dashed line for each OPV material.

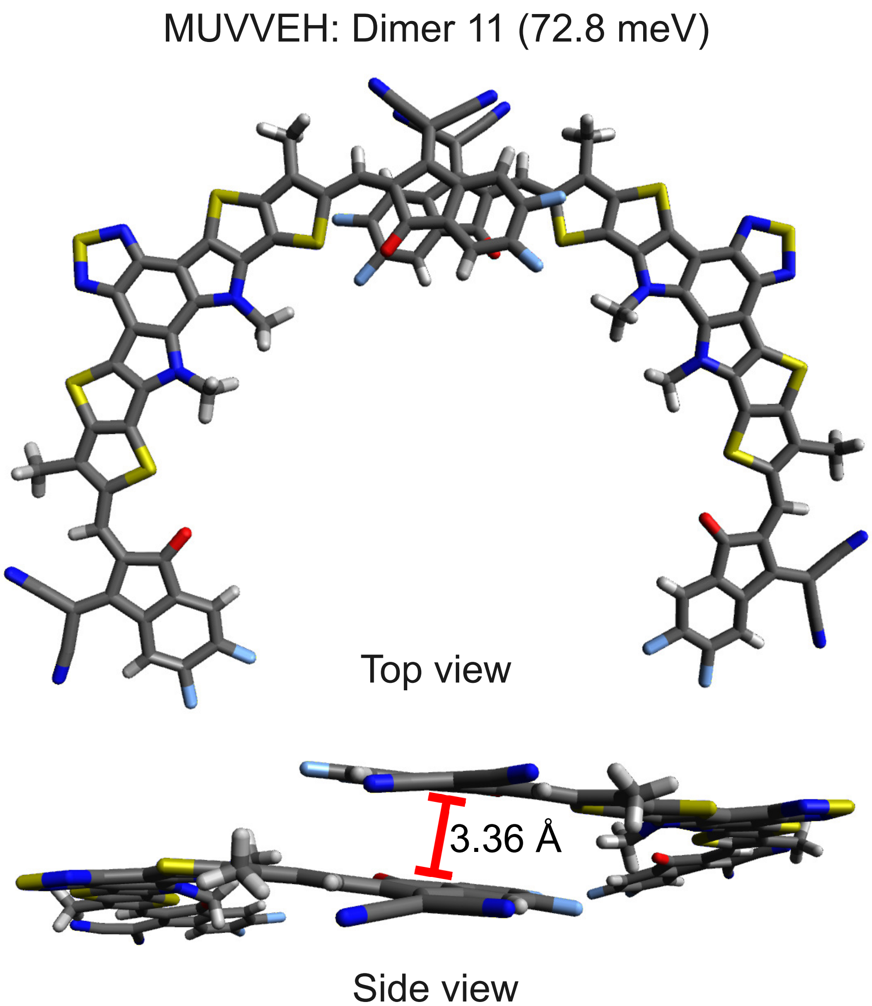

Figure S7: Dimer 11 in the Y6 crystal with CCDC ID: MUVVEH. This dimer exceeds the incoherent limit.

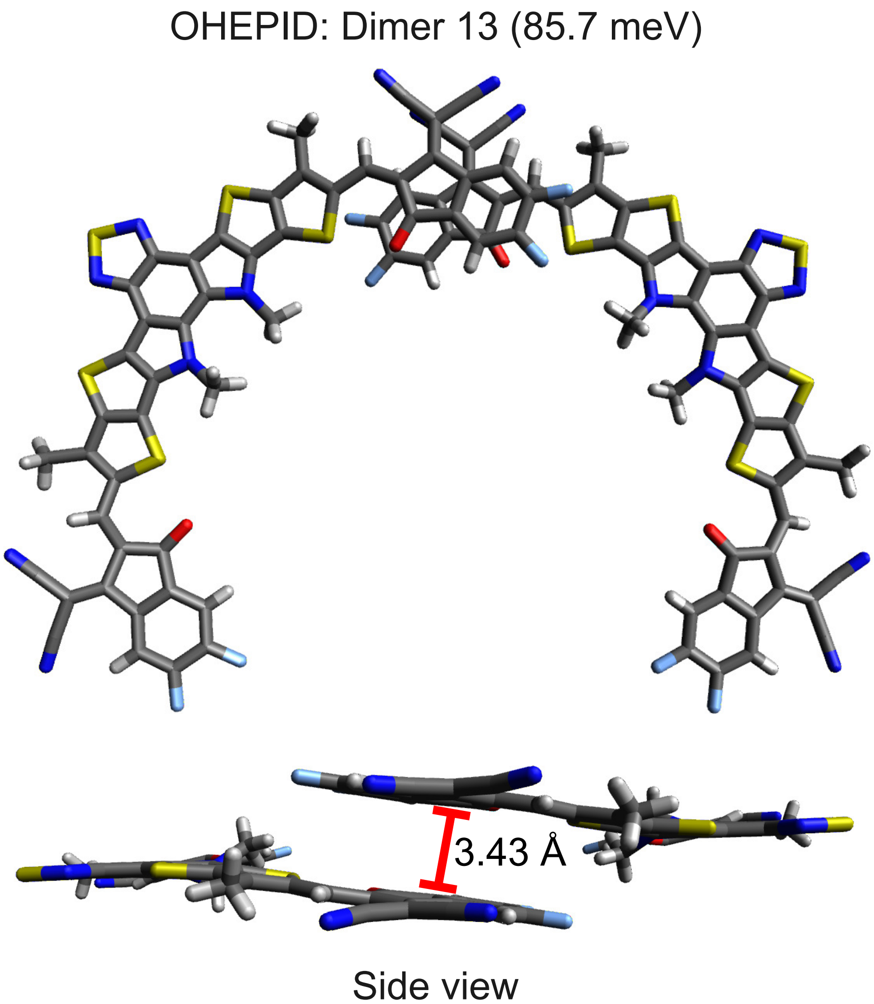

Figure S8: Dimer 13 in the Y6 crystal with CCDC ID: OHEPID. This dimer exceeds the incoherent limit.

Table S2: The energetic components of the EET calculation for two Y6 dimers in two different crystals. These dimers exceeded the incoherent limit for Y6. Note that the Coulombic component of the EET calculation is equivalent to the ATC coupling value.

Crystal CCDC ID	Dimer Number	Energetic Contributions from EET (meV)				Total Coupling (meV)
		Coulombic	Exact -Exchange	Exchange -Correlation	Overlap Contribution	
MUVVEH	11	64.3	-0.1	-0.1	8.8	72.9
OHEPID	13	56.0	-0.1	-0.1	29.9	85.8

S4 Kinetic Monte Carlo vs. experimental diffusion coefficient for various coupling disorders σ_V

Figure S9 shows the exciton diffusion coefficients obtained using the Kinetic Monte-Carlo (kMC) algorithm for a range of coupling disorder σ_V between 0 % and 50 % of the coupling values V_{ij}, compared with experimentally obtained exciton diffusion coefficients. These simulations were performed using a combination of short-range EET and long-range $\epsilon_r = 4/5$ ATC coupling values. This figure is equivalent to Figure 4 in the main text, however the error bars in Figure S10 represent the diffusion coefficients for a range of σ_V between 0 % and 50 % of the coupling values V_{ij}.

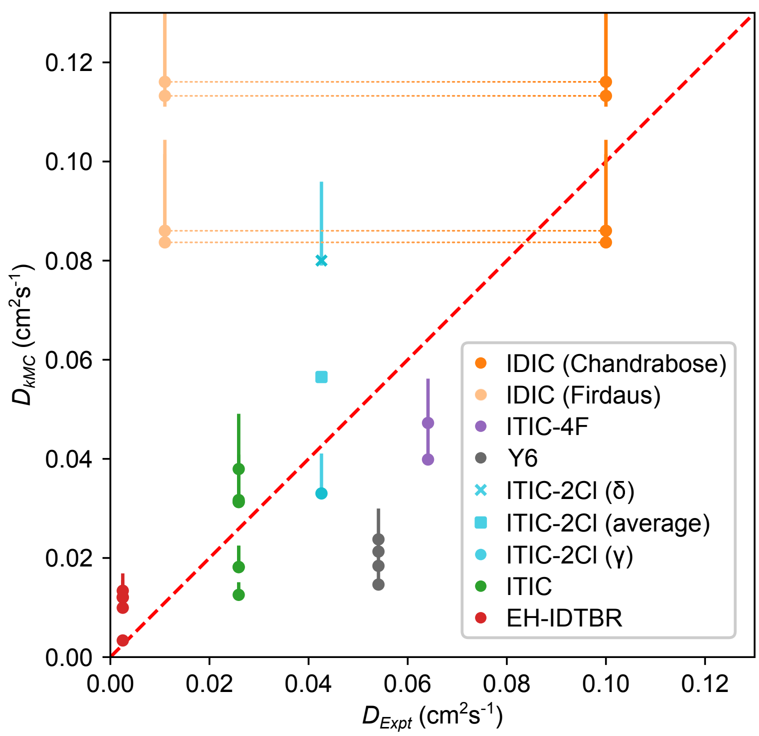

Figure S9: Kinetic Monte-Carlo (kMC) vs. experimental diffusion coefficients (D_{kMC} vs. D_{Expt}) for a series of FREAs (representing 24 crystal structures). Dots represent the exciton diffusion coefficient for coupling disorder $\sigma_V = 0$ (0 %), while the error bars show the range of exciton diffusion coefficients obtained for various values of σ_V between 0 % to 50 % of the coupling values V_{ij}. Points closer to the dashed red line indicate better agreement between the predicted and experimental diffusion rates. Dots of the same colour represent different crystal structures for the same FREA material. The dotted orange lines indicate that both sets of orange points are experimental IDIC measurements from different groups.

S5 Kinetic Monte-Carlo vs. experimental diffusion coefficients with only ATC coupling values

Figure S10 shows the Kinetic Monte-Carlo (kMC) vs. experimental diffusion coefficients for a series of FREAs using only short-range $\epsilon_r = 1$ ATC and long-range $\epsilon_r = 4/5$ ATC coupling values. This is unlike Figure 4, which shows the kMC vs. experimental diffusion coefficients using a combination of short-range EET and long-range $\epsilon_r = 4/5$ ATC coupling values.

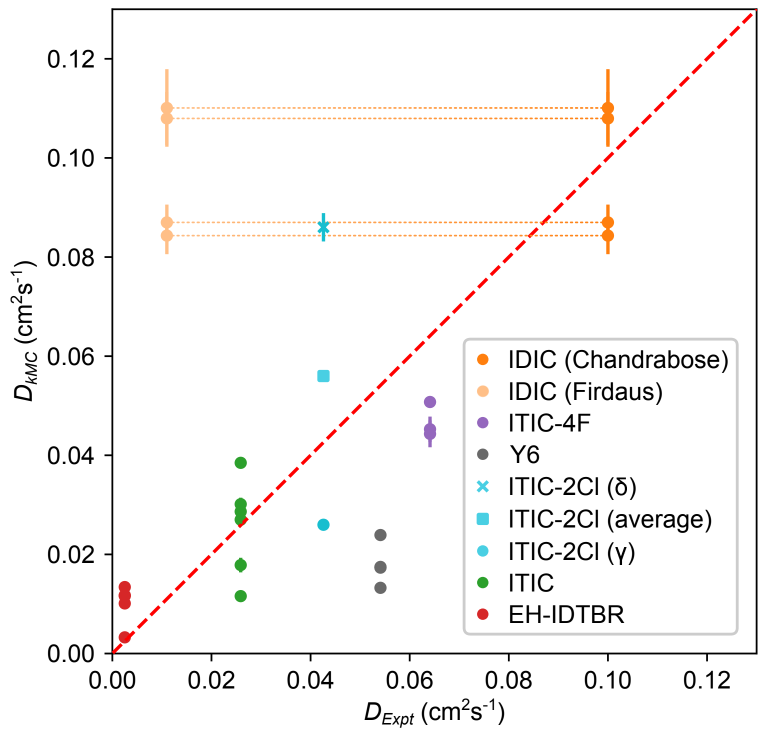

Figure S10: Kinetic Monte-Carlo (kMC) vs. experimental diffusion coefficients (D_{kMC} vs. D_{Expt}) for a series of FREAs shown in Figure 3 (representing 24 crystal structures). The kMC simulations was used with purely ATC coupling values. Points closer to the dashed red line indicate better agreement between the predicted and experimental diffusion rates. Dots of the same colour represent different crystal structures for the same FREA material. The dotted orange lines indicate that both sets of orange points are experimental IDIC measurements from different groups. Error bars show 3× the standard deviation.

S6 The analytic sum-over-rates diffusion rate model

S6.1 Derivation

The following section describes the derivation for the analytic sum-over-rates diffusion rate model given Section 3.2 of this paper (Equations 8 to 10).

S6.1.1 Defining a single-hop diffusion coefficient

The sum-over-rates (SOR) diffusion coefficient D_{SOR} is an approximation to the diffusion coefficient D defined by Equation 7 in the main text. In contrast to kMC simulations, which compute D via averaging the cumulative squared displacement over many exciton trajectories, the SOR approach considers a single average exciton transfer event ('hop') from a central molecule to one of its neighbours. Specifically, we define D_{SOR} as the ratio of the average square displacement of a single hop $\langle r^2 \rangle$ to the average hop time $\langle t \rangle$, multiplied by a factor involving the dimensionality n ($n = 3$ in the present work):

$$D_{SOR} = \frac{1}{2n} \frac{\langle r^2 \rangle}{\langle t \rangle} \tag{S1}$$

There are three types of averaging present in this equation. First, there is averaging over the intrinsic variability in hopping rates and distances, because even a fixed rate constant k only defines the distribution that hop times are drawn from, not the individual hop times themselves. We account for this variation by using the average hop time $\langle t(k) \rangle = 1/k$. For a molecule l with a set of N neighbouring molecules $j = 1, 2, ..., N$, the average hopping time for an exciton to hop from molecule l to a neighbouring molecule is $\langle t_l \rangle = 1/k_{total,l}$, where the total rate constant for exciton transfer, $k_{total,l}$, is calculated as the sum of the individual rate constants $k_{l1}, k_{l2}, ..., k_{lN}$, that is $k_{total,l} = \sum_{j=1}^{N} k_{lj}$. Similarly, hops to different neighbouring molecules correspond to different distances. The average hopping distance for an exciton to hop from molecule l to a neighbouring molecule is given by the distance of the hop, multiplied by the probability that hop occurs, giving $\langle r_l^2 \rangle = \sum_{j=1}^{N} P_{lj} r_{lj}^2$. The probability P_{lj} that the exciton is transferred to neighbour j is given by $P_{lj} = k_{lj}/k_{total,l}$. This results in the following expression for $D_{l,SOR}$, the SOR diffusion coefficient for hops starting from molecule l as a function of the rate constants $k_{l1}, k_{l2}, ..., k_{lN}$:

$$\begin{aligned} D_{l,SOR}(k_{l1}, k_{l2}, ..., k_{lN}) &= \frac{1}{2n} k_{total,l} \sum_{j=1}^{N} P_{lj} r_{lj}^2 \\ &= \frac{1}{2n} k_{total,l} \sum_{j=1}^{N} \frac{k_{lj}}{k_{total,l}} r_{lj}^2 \\ &= \frac{1}{2n} \sum_{j=1}^{N} k_{lj} r_{lj}^2 \end{aligned} \tag{S2}$$

This equation is similar, but not identical, to previously published expressions.[20,21] For Equation (S2), r_{lj} is the distance between the centre of masses of molecules l and j, and the sum includes all molecules j that are within a distance of 40.0 Å from molecule l.

The second type of averaging accounts for the fact that there are different sites within the lattice, due to the presence of symmetrically inequivalent molecules ('lattice positions') in the crystal structures. To account for distinct lattice positions, we first calculate $D_{l,SOR}$ for each lattice position l, which are then averaged according to the procedure described in Section S6.2.

The third type of averaging accounts for variations between molecules in the crystal due to structural/energetic disorder. Our approach for averaging the effect of energetic disorder across molecules in the crystal is described in the following section.

S6.1.2 Effects of energetic disorder

The rate of exciton transfer from a molecule l to a neighbouring molecule j depends on the energy of the exciton before and after the hop. The site energy E_i, is defined as the energy of the exciton when localised on a particular molecule i. Based on the central limit theorem, the probability distribution (ρ) of molecule j having a site energy of E_j can be described by a Gaussian probability density function. We define the energy scale so that ρ is centred around the average site energy, μ_E (i.e. setting $\mu_E = 0$), and the standard deviation is, by definition, equal to the energetic disorder σ_E:

$$\rho\left(E_j, \sigma_E\right) = \frac{1}{\sigma_E\sqrt{2\pi}} \exp\left[-\frac{1}{2}\left(\frac{E_j}{\sigma_E}\right)^2\right] \tag{S3}$$

The exciton transfer rate depends on both the energy of the initial site l, and those of its neighbouring molecules $j = 1, 2, ..., N$. For the initial site l, we take this dependence into account by setting:

$$E_l = \mu_E - \frac{\sigma_E^2}{k_B T} = -\frac{\sigma_E^2}{k_B T} \tag{S4}$$

which is the expectation value for the exciton energy at thermal (quasi-)equilibrium.[22] Here, we assume that the diffusion coefficient is dominated by hops that occur after the exciton has reached equilibrium, which means that the exciton is more likely to be located on a molecule/site with an energy lower than the average site energy.

We account for the variation in site energies of the surrounding molecules by averaging $D_{l,SOR}$ over all possible energies E_j. It is important to note that this averaging procedure is an approximation. Strictly speaking, according to Equation (S1), one should average over different site energies to give $\langle r^2 \rangle$ and $\langle t \rangle$ before calculating D_{SOR}. Adopting this approximation significantly simplifies the problem, while still providing reasonably accurate results for the examples studied in this paper. Because the rate constant $k_{lj}(E_l, E_j)$ depends only on E_l and E_j, this procedure gives:

$$D_{l,SOR} = \frac{1}{2n} \sum_{j=1}^{N} \langle k_{lj} \rangle \, r_{lj}^2 \tag{S5}$$

where $\langle k_{lj} \rangle$ is the average rate constant k_{lj} for exciton transfer from l to j, weighted over different site energies E_j:

$$\langle k_{lj} \rangle = \int_{-\infty}^{\infty} \rho \left(E_j \right) k_{lj} \left(E_j \right) dE_j \tag{S6}$$

S6.1.3 Marcus theory

As in the main text, rate constants for exciton transfer from molecule l to molecule j were calculated using Marcus theory:[17,23,24]

$$k_{lj}^{Marcus} = \frac{2\pi}{\hbar} \left| V_{lj} \right|^2 \frac{1}{\sqrt{4\pi\lambda k_b T}} \exp \left(- \frac{\left(\Delta E_{lj} + \lambda \right)^2}{4\lambda k_b T} \right) \tag{S7}$$

where V_{lj} is the excitonic coupling between l and j, λ is the reorganisation energy of the FREA of interest, $\hbar$ is the reduced Planck constant, k_b is Boltzmann's constant, and T is the absolute temperature (set to $T = 300$ K in this work). $\Delta E_{lj} = E_j - E_l$ is the change in energy when an exciton hops from molecule l to molecule j.

With E_l defined by Equation (S4), Equation (S7) becomes:

$$k_{lj}^{Marcus} = \frac{2\pi}{\hbar} \left| V_{lj} \right|^2 \frac{1}{\sqrt{4\pi\lambda k_b T}} \exp \left(- \frac{\left(E_j + \frac{\sigma_E^2}{k_b T} + \lambda \right)^2}{4\lambda k_b T} \right) \tag{S8}$$

S6.1.4 Average rate constant for a thermalised exciton

An explicit expression for the average rate constant for an exciton to hop between molecules l and j is obtained by substituting Equation (S3) and Equation (S8) into Equation (S6):

$$\begin{aligned}
\langle k_{lj} \rangle &= \int_{-\infty}^{\infty} \rho\left(E_j\right) k_{lj}\left(E_j\right) dE_j \\
&= \int_{-\infty}^{\infty} \frac{1}{\sigma_E \sqrt{2\pi}} \exp\left[-\frac{1}{2}\left(\frac{E_j}{\sigma_E}\right)^2\right] \times \frac{2\pi}{\hbar} \left|V_{lj}\right|^2 \frac{1}{\sqrt{4\pi\lambda k_b T}} \exp\left[-\frac{\left(E_j + \frac{\sigma_E^2}{k_b T} + \lambda\right)^2}{4\lambda k_b T}\right] dE_j \\
&= \frac{\left|V_{lj}\right|^2}{\sigma_E \hbar \sqrt{2\lambda k_b T}} \int_{-\infty}^{\infty} \exp\left[-\frac{1}{2}\left(\frac{E_j}{\sigma_E}\right)^2\right] \exp\left[-\frac{\left(E_j + \frac{\sigma_E^2}{k_b T} + \lambda\right)^2}{4\lambda k_b T}\right] dE_j
\end{aligned} \tag{S9}$$

Equation (S9) is a convolution of two Gaussians, which has the solution:

$$\int_{-\infty}^{\infty} e^{-at^2} e^{-b(t-x)^2} dt = \sqrt{\frac{\pi}{a+b}} e^{-\frac{ab}{a+b}x^2} \tag{S10}$$

This gives Equation (S11):

$$\langle k_{lj} \rangle = \left|V_{lj}\right|^2 \times \frac{1}{\hbar} \sqrt{\frac{4\pi}{2\sigma_E^2 + 4\lambda k_b T}} \exp\left[-\frac{\left(\lambda + \frac{\sigma_E^2}{k_b T}\right)^2}{2\sigma_E^2 + 4\lambda k_b T}\right] \tag{S11}$$

We can simplify this expression by moving all the constants that are not specific to molecule j into a term called $I\left(\sigma_E, \lambda, T\right)$:

$$I\left(\sigma_E, \lambda, T\right) = \frac{1}{\hbar} \sqrt{\frac{4\pi}{2\sigma_E^2 + 4\lambda k_b T}} \exp\left[-\frac{\left(\lambda + \frac{\sigma_E^2}{k_b T}\right)^2}{2\sigma_E^2 + 4\lambda k_b T}\right] \tag{S12}$$

With this definition, Equation (S11) becomes:

$$\langle k_{lj} \rangle = \left|V_{lj}\right|^2 I\left(\sigma_E, \lambda, T\right) \tag{S13}$$

S6.1.5 Analytical sum-over-rates diffusion rate model

Substituting Equation (S13) into Equation (S5) gives the analytical sum-over-rates diffusion rate model, Equation (S14):

$$D_{l,SOR} = \frac{1}{2n} I\left(\sigma_E, \lambda, T\right) \sum_{j=1}^{N} \left|V_{lj}\right|^2 r_{lj}^2 \tag{S14}$$

S6.2 Obtaining quasi-steady state occupation probabilities, $\{p_l\}$, and calculating the overall analytical sum-over-rates diffusion coefficient for the crystal, D_{SOR}

The overall analytical sum-over-rates diffusion rate model, D_{SOR}, can be evaluated by taking $D_{l,SOR}$ for each environmentally unique site l, and multiplying it by the quasi-steady state occupation probability for that site, p_l:

$$D_{SOR} = \sum_{l} p_l D_{l,SOR} \tag{S15}$$

The quasi-steady state occupation probability (p_l) can be obtained by first constructing a matrix $\mathbf{P}$ containing the exciton hopping probabilities for an exciton hopping from one environmentally unique site, l, to another environmentally unique site, m, for all unique sites from 1 to L:

$$\mathbf{P} = \{p_{l \to m}\} = \begin{pmatrix} p_{1\to1} & p_{2\to1} & \cdots & p_{L\to1} \\ p_{1\to2} & p_{2\to2} & \cdots & p_{L\to2} \\ \vdots & \vdots & \ddots & \vdots \\ p_{1\to L} & p_{2\to L} & \cdots & p_{L\to L} \end{pmatrix} \tag{S16}$$

The steady state solution for $\mathbf{P}$ can be obtained by multiplying $\mathbf{P}$ by a probability vector $\bar{\mathrm{p}}$ that contains all the probabilities for an exciton to be located on one of the environmentally unique sites in the crystal, $\{p_l\}$. The steady state solution is defined as a solution that gives the same vector $\bar{\mathrm{p}}$ when multiplied by $\mathbf{P}$, Equation (S17):

$$\mathbf{P}\bar{\mathrm{p}}_n = \bar{\mathrm{p}}_{n+1} = \bar{\mathrm{p}}_n \tag{S17}$$

Rearranging Equation (S17) gives Equation (S18):

$$(\mathbf{P} - \mathbf{I})\,\bar{\mathrm{p}} = \mathbf{0} \tag{S18}$$

In practise, this can be solved using an eigen-equation solver algorithm, and taking the eigenvector for the solution giving an eigenvalue of 1. Note that by definition, the sum of each column in $\mathbf{P}$ is equal to 1. This is because each column describes all the ways an exciton hops out of unique site l (including itself), which sums up to 100 %. It is this fact that means that $\mathbf{P}$ will have an eigenvalue of 1.

S7 Details of the EET coupling values

The excel files "EET_Data_by_crystal.xlsx" and "All_EET_Data.xlsx" contains details about the energetic components of the EET coupling values, including the Coulombic components of the EET coupling values. The "All_EET_Data.xlsx" file also contains ATC coupling values for comparison with EET. The XYZ files for the molecules and dimers that coupling values have been obtained for are given in "xyz_files.zip" to allow the user to see the distance and spatial relationship between molecules in the dimers.

References

(1) Bristow, H.; Thorley, K. J.; White, A. J. P.; Wadsworth, A.; Babics, M.; Hamid, Z.; Zhang, W.; Paterson, A. F.; Kosco, J.; Panidi, J.; Anthopoulos, T. D.; McCulloch, I. Impact of Nonfullerene Acceptor Side Chain Variation on Transistor Mobility. *Adv. Electron. Mater.* **2019**, *5*, 1–11, DOI: `10.1002/aelm.201900344`.

(2) Che, Y.; Zhang, Y.; Yang, Y.; Liu, C.-H.; Izquierdo, R.; Xiao, S. S.; Perepichka, D. F. Understanding the Photovoltaic Behavior of A–D–A Molecular Semiconductors through a Permutation of End Groups. *J. Org. Chem.* **2019**, *85*, 52–61, DOI: `10.1021/acs.joc.9b01654`.

(3) Halaby, S.; Martynowycz, M. W.; Zhu, Z.; Tretiak, S.; Zhugayevych, A.; Gonen, T.; Seifrid, M. Microcrystal Electron Diffraction for Molecular Design of Functional Non-Fullerene Acceptor Structures. *Chem. Mater.* **2021**, *33*, 966–977, DOI: `10.1021/acs.chemmater.0c04111`.

(4) Chandrabose, S.; Chen, K.; Barker, A. J.; Sutton, J. J.; Prasad, S. K. K.; Zhu, J.; Zhou, J.; Gordon, K. C.; Xie, Z.; Zhan, X.; Hodgkiss, J. M. High Exciton Diffusion Coefficients in Fused Ring Electron Acceptor Films. *J. Am. Chem. Soc.* **2019**, *141*, 6922–6929, DOI: `10.1021/jacs.8b12982`.

(5) Mondelli, P.; Boschetto, G.; Horton, P. N.; Tiwana, P.; Skylaris, C.-K.; Coles, S. J.; Krompiec, M.; Morse, G. Meta-analysis: the molecular organization of non-fullerene acceptors. *Mater. Horiz.* **2020**, *7*, 1062–1072, DOI: `10.1039/c9mh01439j`.

(6) Zhu, L.; Yang, C.; Yi, Y.; Wei, Z. Effective Modulation of Exciton Binding Energies in Polymorphs of a Small-Molecule Acceptor for Organic Photovoltaics. *J. Phys. Chem. Lett.* **2020**, *11*, 10227–10232, DOI: `10.1021/acs.jpclett.0c03260`.

(7) Han, G.; Guo, Y.; Song, X.; Wang, Y.; Yi, Y. Terminal π–π stacking determines three-dimensional molecular packing and isotropic charge transport in an A–π–A electron

acceptor for non-fullerene organic solar cells. *J. Mater. Chem. C* **2017**, *5*, 4852–4857, DOI: 10.1039/c7tc01310h.

(8) Zhou, J.; Wen, X.; Tang, N.; Zhou, X.; Wang, C.; Zheng, N.; Liu, L.; Xie, Z. Ultrafast and Long-Range Exciton Migration through Anisotropic Coulombic Coupling in the Textured Films of Fused-Ring Electron Acceptors. *J. Phys. Chem. Lett.* **2020**, *11*, 7908–7913, DOI: 10.1021/acs.jpclett.0c02569.

(9) Aldrich, T. J.; Matta, M.; Zhu, W.; Swick, S. M.; Stern, C. L.; Schatz, G. C.; Facchetti, A.; Melkonyan, F. S.; Marks, T. J. Fluorination Effects on Indacenodithienothiophene Acceptor Packing and Electronic Structure, End-Group Redistribution, and Solar Cell Photovoltaic Response. *J. Am. Chem. Soc.* **2019**, *141*, 3274–3287, DOI: 10.1021/jacs.8b13653.

(10) Swick, S. M.; Gebraad, T.; Jones, L.; Fu, B.; Aldrich, T. J.; Kohlstedt, K. L.; Schatz, G. C.; Facchetti, A.; Marks, T. J. Building Blocks for High-Efficiency Organic Photovoltaics: Interplay of Molecular, Crystal, and Electronic Properties in Post-Fullerene ITIC Ensembles. *ChemPhysChem* **2019**, *20*, 2608–2626, DOI: 10.1002/cphc.201900793.

(11) Lin, F.; Jiang, K.; Kaminsky, W.; Zhu, Z.; Jen, A. K.-Y. A Non-fullerene Acceptor with Enhanced Intermolecular π-Core Interaction for High-Performance Organic Solar Cells. *J. Am. Chem. Soc.* **2020**, *142*, 15246–15251, DOI: 10.1021/jacs.0c07083.

(12) Lai, H.; Chen, H.; Zhou, J.; Qu, J.; Chao, P.; Liu, T.; Chang, X.; Zheng, N.; Xie, Z.; He, F. Isomer-free: Precise Positioning of Chlorine-Induced Interpenetrating Charge Transfer for Elevated Solar Conversion. *iScience* **2019**, *17*, 302–314, DOI: 10.1016/j.isci.2019.06.033.

(13) Zhang, G. et al. Delocalization of exciton and electron wavefunction in non-fullerene

acceptor molecules enables efficient organic solar cells. *Nat. Commun.* **2020**, *11*, 1–10, DOI: 10.1038/s41467-020-17867-1.

(14) Zhu, W. et al. Crystallography, Morphology, Electronic Structure, and Transport in Non-Fullerene/Non-Indacenodithienothiophene Polymer:Y6 Solar Cells. *J. Am. Chem. Soc.* **2020**, *142*, 14532–14547, DOI: 10.1021/jacs.0c05560.

(15) Zhu, L.; Zhang, J.; Guo, Y.; Yang, C.; Yi, Y.; Wei, Z. Small Exciton Binding Energies Enabling Direct Charge Photogeneration Towards Low-Driving-Force Organic Solar Cells. *Angew. Chem. Int. Ed.* **2021**, *60*, 15348–15353, DOI: https://doi.org/10.1002/anie.202105156.

(16) Refaely-Abramson, S.; Jain, M.; Sharifzadeh, S.; Neaton, J. B.; Kronik, L. Solid-state optical absorption from optimally tuned time-dependent range-separated hybrid density functional theory. *Phys. Rev. B* **2015**, *92*, 081204, DOI: 10.1103/PhysRevB.92.081204.

(17) Firdaus, Y. et al. Long-range exciton diffusion in molecular non-fullerene acceptors. *Nat. Commun.* **2020**, *11*, 1–10, DOI: 10.1038/s41467-020-19029-9.

(18) Classen, A.; Chochos, C. L.; Lüer, L.; Gregoriou, V. G.; Wortmann, J.; Osvet, A.; Forberich, K.; McCulloch, I.; Heumüller, T.; Brabec, C. J. The role of exciton lifetime for charge generation in organic solar cells at negligible energy-level offsets. *Nat. Energy* **2020**, *5*, 711–719, DOI: 10.1038/s41560-020-00684-7.

(19) Hume, P. A.; Jiao, W.; Hodgkiss, J. M. Long-range exciton diffusion in a non-fullerene acceptor: approaching the incoherent limit. *J. Mater. Chem. C* **2021**, *9*, 1419–1428, DOI: 10.1039/D0TC05697A.

(20) Wang, L.; Nan, G.; Yang, X.; Peng, Q.; Li, Q.; Shuai, Z. Computational methods for design of organic materials with high charge mobility. *Chem. Soc. Rev.* **2010**, *39*, 423–434, DOI: 10.1039/b816406c.

(21) Deng, W.-Q.; Goddard, W. A. Predictions of Hole Mobilities in Oligoacene Organic Semiconductors from Quantum Mechanical Calculations. *J. Phys. Chem. B* **2004**, *108*, 8614–8621, DOI: 10.1021/jp0495848.

(22) Bässler, H. Charge Transport in Disordered Organic Photoconductors a Monte Carlo Simulation Study. *Phys. Status Solidi B* **1993**, *175*, 15–56, DOI: 10.1002/pssb.2221750102.

(23) Aragó, J.; Troisi, A. Regimes of Exciton Transport in Molecular Crystals in the Presence of Dynamic Disorder. *Adv. Funct. Mater.* **2015**, *26*, 2316–2325, DOI: 10.1002/adfm.201503888.

(24) Londi, G.; Dilmurat, R.; D'Avino, G.; Lemaur, V.; Olivier, Y.; Beljonne, D. Comprehensive modelling study of singlet exciton diffusion in donor–acceptor dyads: when small changes in chemical structure matter. *Phys. Chem. Chem. Phys.* **2019**, *21*, 25023–25034, DOI: https://doi.org/10.1039/C9CP05201A.